JOURNAL OF PROPULSION AND POWER
Vol. 34, No. 4, July–August 2018

Hollow Cathode Simulations with a First-Principles Model of Ion-Acoustic Anomalous Resistivity

Alejandro Lopez Ortega*
Jet Propulsion Laboratory, California Institute of Technology, Pasadena, California 91109
Benjamin A. Jorns†
University of Michigan, Ann Arbor, Michigan 48109
and
Ioannis G. Mikellides‡
Jet Propulsion Laboratory, California Institute of Technology, Pasadena, California 91109

DOI: 10.2514/1.B36782

A mathematical model of the ion–acoustic turbulence that is known to develop in the plume of hollow cathodes is presented. The model takes the form of a partial differential equation for the ion–acoustic wave energy density that can be solved concurrently with a set of the equations of motion that have been augmented with anomalous terms to account for the ion–acoustic turbulence-driven transport of momentum and heat for electrons and ions. Numerical simulations in two-dimensional axisymmetric geometry that solve the complete system of these equations show significantly better agreement with plasma measurements compared to a previous idealized model, which assumed complete saturation of the ion–acoustic turbulence and did not account for the growth stage of the waves. In particular, the model is able to predict accurately the location and magnitude of the maximum resistivity to the electron current along the cathode centerline.

Nomenclature

B	=	magnetic field (magnitude)
$\boldsymbol{B}$	=	magnetic field (vector)
c	=	sound speed
$\boldsymbol{E}$	=	electric field vector
$\boldsymbol{F}$	=	force
f	=	distribution function
$\boldsymbol{j}$	=	current density vector
k	=	wavelength (magnitude)
$\boldsymbol{k}$	=	wavelength (vector)
$\hat{\boldsymbol{k}}$	=	wavelength (direction vector)
L_{emitter}	=	emitter length
M	=	Mach number
m	=	molecular mass
N_k	=	wave action for the kth mode
n	=	number density
$\dot{n}$	=	ionization rate
p	=	pressure
Q	=	volumetric heating
Q^T	=	thermal equilibration term
q	=	electron charge
r	=	coordinate in radial direction
T	=	temperature
T_w	=	emitter wall temperature
t	=	time
$\boldsymbol{u}$	=	drift velocity vector
$\hat{V}_D$	=	relative drift direction between electrons and ions
v	=	thermal velocity
W_k	=	wave energy density for the kth mode
W_T	=	wave energy density
W_0	=	floor value of the wave energy density
z	=	coordinate in axial direction
α, α'	=	parameters in Sagdeev–Galeev model
$\boldsymbol{\beta}$	=	unitary vector in direction of magnetic field
ϵ_{ip}	=	ionization potential
ϵ_k	=	energy density of the electrostatic potential for the kth mode
ϵ_0	=	vacuum permittivity
η	=	resistivity
θ	=	coordinate in azimuthal direction
κ	=	thermal conductivity
λ_D	=	Debye length
μ_0	=	vacuum permeability
ν	=	collision frequency
$\boldsymbol{\tau}$	=	viscous stress tensor
ϕ	=	plasma potential
Ω	=	Hall parameter
ω	=	frequency of oscillation
ω_i	=	imaginary part of frequency of oscillation
ω_p	=	plasma frequency
ω_r	=	real part of frequency of oscillation

Subscripts

a	=	anomalous
e	=	electron
i	=	ion
n	=	neutral
0	=	zeroth-order term in linear decomposition
1	=	first-order term in linear decomposition
//	=	parallel to magnetic field
$\perp$	=	perpendicular to magnetic field

Presented as Papers 2016-4626 and 2016-4627 at the 52nd AIAA/SAE/ASEE Joint Propulsion Conference, Salt Lake City, UT, 25–27 July 2016; received 1 June 2017; revision received 20 December 2017; accepted for publication 8 January 2018; published online 19 February 2018.

*Member of the Technical Staff, Electric Propulsion Group, 4800 Oak Grove Drive, Mail Stop 125-109. Member AIAA.
†Assistant Professor, Department of Aerospace Engineering, 1320 Beal Avenue. Member AIAA.
‡Principal Engineer, Electric Propulsion Group, 4800 Oak Grove Drive Mail Stop 125-109. Associate Fellow AIAA.

I. Introduction

ELECTRIC propulsion systems have recently been proposed as the main propulsion source for deep-space exploration missions. As an example, the Asteroid Robotic Redirect Mission

(ARRM) concept would make use of Hall thrusters and have power and operating time requirements in the order of 30 kW and 30,000 h, respectively [1,2]. All the components of the electric propulsion system, including the hollow cathodes that act as the source of electrons for plasma propulsion devices, must be qualified to meet mission requirements. The path to qualification through predictive modeling most recently has been identified as a tool for assessing the ion propulsion system for ARRM because validated models can help overcome concerns associated with qualification through ground testing, such as the problem of facility effects and high costs incurred by long-duration tests. Predictive modeling of hollow cathodes must be able to address the multiple failure mechanisms that have been observed in experimental testing. A well-known failure mechanism in hollow cathodes is the erosion of the cathode keeper (a metallic piece that protects the cathode structure from ion bombardment) [3,4]. The principal cause of keeper erosion has been identified as the sputtering by ions with energies that exceed the discharge voltage [5]. Thus, keeper erosion has been prevented in the past by employing materials with lower sputtering yield and by operating at flow rates and discharge currents that prohibit "plume mode", a condition whose characteristic feature is the presence of large global oscillations in the plume of the cathode. Even though the driving mechanism for plume mode is not completely understood, it has been shown experimentally that it can be avoided by increasing the mass flow of propellant gas into the cathode. Although the employment of these techniques produced successful results in low-current cathodes (less than 20 A), it has been unclear until recently how the required increase in generated current imposed by high-power space exploration missions would affect the degradation mechanisms in hollow cathodes. Other observed failure mechanisms in hollow cathodes include erosion of the cathode orifice and emitter depletion [6–12].

Driven largely by a need to understand the evolution of the partially ionized gas inside hollow cathodes, which is inherently difficult to access with diagnostics, development of the Orificed Cathode 2D (OrCa2D) code began in the mid-2000s [6,12–15]. The largely collisional plasma inside most electric propulsion hollow cathodes lends itself to a continuum description of the conservation laws, as confirmed by several results of OrCa2D simulations having been validated by plasma measurements [5,6,12,13,15–17]. The near-plume region of these devices, however, has proven more difficult to capture accurately. The first efforts to model the plume with OrCa2D revealed that electron resistivity due to classical collisions are orders of magnitude too low to explain the measured plasma parameters. Mikellides et al. [13] postulated that the presence of anomalous resistivity in the plume of a hollow cathode was required to explain the rise of the plasma potential and electron temperature measured downstream of the orifice of a cathode operating at 25 A. It was also pointed out in [6,17] by means of numerical simulations and analysis of the same cathode that the conditions for growth of ion–acoustic turbulence (IAT) [18–21] existed downstream of the orifice exit and that, when an idealized anomalous resistivity model for the electrons subjected to IAT was included, the agreement with the measurements near the orifice improved significantly. The idealized model was based on the formulations of Sagdeev and Galeev [22] who assumed that the IAT saturates through nonlinear wave-particle interactions, enabling them to reduce the anomalous collision frequency to a simple algebraic function of the macroscopic plasma parameters. Subsequently, the use of the Sagdeev and Galeev formulation in OrCa2D led to the correct modeling of experimentally measured plasma parameters along the centerlines of the NSTAR [5] and NEXIS cathodes [13], operating at maximum discharge currents of 13.3 and 27.5 A, respectively, as well as a 100 A LaB_6 laboratory cathode [15], although in this case, the agreement was mostly qualitative. The presence of IAT in the near plume of hollow cathodes was later confirmed experimentally for the first time in a high-current lanthanum hexaboride (LaB_6) cathode as reported by Jorns et al. [23].

Even though the Sagdeev and Galeev IAT model appeared to capture well the IAT-driven anomalous transport in low-current cathodes, our most recent work indicates that OrCa2D captures plasma trends only qualitatively in higher-current cathodes. This suggests that the assumptions that led to the Sagdeev and Galeev scaling of the anomalous collision frequency fail at higher currents. Thus, it is necessary to develop a more sophisticated model that self-consistently captures the evolution of the IAT in the cathode plume. A major motivation for a more accurate model is that IAT can lead to the formation of a high-energy tail in the distribution function of the ions [23,24]. These high-energy ions can produce erosion of the keeper surface. In attempts to mitigate such erosion, a parametric study of the magnitude of the turbulence as a function of the discharge current and mass flow rate of xenon performed by Jorns et al. [25] identified a range of mass flow rates at discharge currents in excess of 25 A within which the amplitude of the turbulent oscillations were minimal.

In this paper, we present a model for the IAT that stems directly from kinetic theory and the notion that waves can be described as quasi particles. The model, presented in Sec. II, takes the form of a partial differential equation (PDE) instead of the algebraic expression based on the Sagdeev–Galeev model [22] used to date. This PDE is solved concurrently with the evolution equations for neutrals, ions, and electrons, already reported in [5,6,12–15]. In this study, we also find that self-induced magnetic fields are not negligible in cathodes operating at large discharge currents. Therefore, Ohm's law for electrons has been modified to account for the azimuthal component of the magnetic field. Comparisons between plasma measurements and numerical results are shown in Sec. III for a high-current LaB_6 cathode operating at 140 A and 10 cm^3. Section IV summarizes the main findings in this paper.

II. Mathematical Model and Numerical Implementation in the OrCa2D Code

The physics models and numerical methods in OrCa2D have been described in detail in [5,6,12–15,26] and will only be described briefly here. OrCa2D solves conservation laws for the three species present in a partially ionized gas: electrons, xenon ions, and xenon neutrals. A time-splitting method in which all the equations are solved consecutively at every time step is employed. Inside the cathode, the Navier–Stokes equations for neutral xenon are solved using an implicit backward Euler scheme, which includes the viscous terms. It has been shown that the flow of neutrals transitions from a low to a high Knudsen number downstream of the cathode orifice. Thus, a fluid approximation is not applicable in the cathode plume. Free molecular flow, in which neutrals move in straight paths, is assumed downstream of an axial location, typically chosen to be in the cathode orifice where the Knudsen number approaches unity. Mass and momentum continuity are preserved across the transition boundary. The Euler equations for mass and momentum of charged ions are solved in the entire computational domain. The presence of ion momentum terms was recently included to account for the increased ion densities and currents in high-current cathodes. The effects of ionization, charge exchange, and electron–ion collisions are considered in the equations and modeled as source or drag terms. The conservation equations for ions are also solved using a backward Euler implicit scheme. Previous studies [14,15] that did not take into account the anomalous heating that ions may undergo have shown that the thermal equilibration time between ions and neutrals is small, which allowed for solving only one energy equation for both ions and neutrals. In this paper, it is shown that anomalous heating of the ions in the plume due to IAT is, in fact, the dominating term in the ion energy equation, and therefore a separate equation is solved. Finally, the plasma parameters for electrons are determined from the solution of the electron energy equation, which also employs a backward Euler scheme, and the combination of the current conservation equation with the vector form of Ohm's law. The resistivity in Ohm's law is determined as a function of the classical collision frequencies (i.e., electron–ion and electron-neutral) and the anomalous collision frequency that models the effect of the IAT on the electron transport. When an external magnetic field is applied, the resistivity is no longer isotropic, with the component perpendicular to the magnetic field dependent on the electron Hall parameter Ω_e.

The choice of an implicit Euler scheme, which is first-order-accurate, for time discretization, is justified by the requirement of

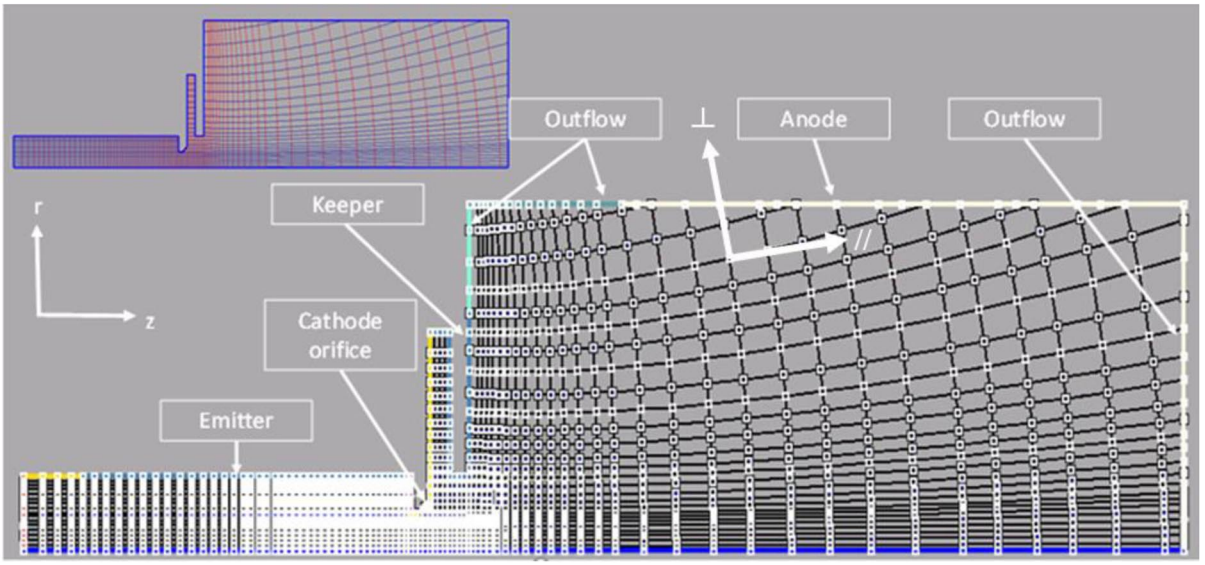

Fig. 1 OrCa2D computational domain and mesh pointing to the different boundary conditions. The mesh in the cathode interior is rectilinear, and an MFAM is used for the plume.

employing sufficiently large time steps that simulations can be run in the time frame of a few hours in workstation computers. Spatial discretization makes use of a Harten–Lax–van Leer (HLL) scheme [27] for convection terms. This method, although first-order-accurate, is able to capture all the possible wave patterns that may occur and can be evaluated implicitly (according to the implicit Euler scheme used for time discretization) [28]. This method is also monotone because it captures discontinuities without numerical oscillations in the solution. Diffusion terms (thermal and electrical conductivity) are evaluated by means of a centered scheme that offers second-order accuracy.

The computational domain (Fig. 1) comprises the interior of the cathode tube and a considerable section (in the order of tens of centimeters) of the plume, which includes the collecting surface of the anode. The computational domain is designed in a way such that it can replicate the exact conditions at which a cathode test was run in the laboratory. Because a magnetic-field-aligned mesh (MFAM) [29,30] simplifies the solution of Ohm's law, the computational mesh can be made aligned to an applied external magnetic field if one existed in the laboratory test or if the aim of the simulation is to understand plasma parameters when the cathode is operated with a Hall thruster. Convergence of the solution as a function of mesh resolution in OrCa2D was shown for the NSTAR cathode in [12].

Boundary conditions need to be imposed at each surface and at the outflow. Boundary conditions for a conductor surface are used at the emitter, orifice, keeper, and anode. These conditions assume an infinitesimally small sheath that can be modeled as one-dimensional. In addition, the total electron current from the emitter is the difference between the emitted and absorbed current. The emitted current is determined by the Richardson–Dursham [31] emission equation. The emitter temperature is specified as an input based on available laboratory measurements.

A. Modeling of the Ion–Acoustic Turbulence

1. *Impact of Electrostatic Turbulence on Macroscopic Parameters*

We estimate the impact of electrostatic oscillations on the macroscopic properties of the ions and electrons by taking moments of a kinetic equation for the plasma. This technique follows the treatment of Dum [32] and Davidson and Krall [33], in which the distribution function in velocity space for each species s in the plasma is the sum of the background distribution $f_{0(s)}$ and a perturbation distribution $f_{1(s)}$. The plasma potential is assumed to admit a similar decomposition, $\phi = \phi_0 + \phi_1$. In addition, we invoke the eikonal approximation to represent the perturbation variables as the sum over modes with frequency ω and wave vector $\boldsymbol{k}$, $f_{1(s)} = \sum_k f_{1k(s)} \exp i(\boldsymbol{k}\cdot\boldsymbol{x} - \omega t)$. Taking moments of the Boltzmann equation and invoking the random phase approximation between modes, we find that the evolution equations for momentum density and energy density [34] are modified in the presence of oscillations by the additional force and energy terms, respectively:

$$\boldsymbol{F}_{a(s)} = -q_s \sum_k \boldsymbol{k}\phi_{1k}\mathrm{Im}[n_{1k(s)}] \tag{1}$$

$$Q_{a(s)} = -q_s \sum_k \phi_{1k}\mathrm{Im}[\omega n_{1k(s)}] \tag{2}$$

Here, we have defined the zeroth moment of the first-order distribution as the perturbed plasma density:

$$n_{1k(s)} = \int f_{1k(s)}\,\mathrm{d}\boldsymbol{v}$$

We can gain insight into how these driving terms for each species in Eqs. (1) and (2) relate to one another by taking the real and imaginary components of Poisson's equation for the kth mode:

$$\mathrm{Im}[n_{1k(i)}] = \mathrm{Im}[n_{1k(e)}],$$
$$Re[n_{1k(i)}] = Re[n_{1k(e)}] + \frac{\varepsilon_0\phi_{1k}k^2}{q} \tag{3}$$

We thus find that total momentum due to the growth and absorption of the electrostatic modes in the plasma is conserved (i.e., $\boldsymbol{F}_{a(i)} = -\boldsymbol{F}_{a(e)}$). Ion–acoustic modes are characterized by oscillations in both particle species as well as electrostatic fields (cf. [20]). Because electrostatic fields have no momentum and the electrons are light, the wave momentum is primarily carried by the oscillations in the species with the most inertia, the ions. An increase in wave momentum thus results in an average increase in momentum of the ions. By the conservation law, this wave growth must be balanced by a loss of the bulk electron momentum.

For the heating terms in Eq. (2), we prescribe that the wave vector $\boldsymbol{k}$ is real, but the frequency of each mode has an imaginary component, $\omega = \omega_r + i\omega_i$, where $\omega_i \ll \omega_r$. The relations in Eq. (3) combined with Eq. (2) thus yield

$$Q_{a(e)} = q\sum_k \phi_{1k}\Big(\omega_r\mathrm{Im}[n_{1k(e)}] + \omega_i Re[n_{1k(e)}]\Big),$$
$$Q_{a(i)} = -\sum_k\Big[q\phi_{1k}\Big(\omega_r\mathrm{Im}[n_{1k(e)}] + \omega_i Re[n_{1k(e)}]\Big) + 2\omega_i\varepsilon_k\Big] \tag{4}$$

where we have defined the total energy density of the electrostatic field for the kth mode,

$$\varepsilon_k = \frac{1}{2} n_o \varepsilon_0 k^2 \phi_{1k}^2 \tag{5}$$

and used quasi neutrality of the background plasma to write $n_{0(e)} = n_{0(i)} = n_0$. The terms in Eq. (4) represent the change in kinetic energy of the electrons and ions associated with the growth, damping, and propagation of the electrostatic waves. Unlike in the case of momentum, however, not only do the ion oscillations have nonnegligible kinetic energy but so too do the electron oscillations and the electric field associated with the waves. Therefore, energy is only conserved by taking into account both the particle kinetic energy and field energy contributions.

To evaluate the previous terms explicitly for the case of ion–acoustic waves, it is necessary to find expressions for the perturbed electron density $n_{1k(e)}$, the real and imaginary components of the mode frequency ω_r and ω_i, the wave vector $\boldsymbol{k}$, and the potential amplitude ϕ_{1k}. These expressions can be derived from the Boltzmann equation in the presence of perturbations and the dispersion relation for the ion–acoustic instability. A Maxwellian distribution function is assumed for background ions and electrons such that the perturbed densities for electrons and ions are written as

$$\begin{aligned} n_{1k(e)} &= \frac{\phi_{1k} n_0}{T_e}\left(1 + i\left(\frac{\pi}{2}\right)^{1/2}\left[\frac{\omega - \boldsymbol{k}\cdot\boldsymbol{u}_e}{k v_e}\right]\right), \\ n_{1k(i)} &= \frac{q\phi_{1k} n_0}{m_i}\left[\left(\frac{k}{\omega - \boldsymbol{k}\cdot\boldsymbol{u}_i}\right)^2 + i\left(\left(\frac{\nu_i}{\omega - \boldsymbol{k}\cdot\boldsymbol{u}_i}\right)\left(\frac{k}{\omega - \boldsymbol{k}\cdot\boldsymbol{u}_i}\right)^2 \right.\right. \\ &\quad \left.\left. + \left(\frac{\pi}{2}\right)^{1/2}\left(\frac{m_i}{qT_i}\right)^{3/2}\frac{\omega - \boldsymbol{k}\cdot\boldsymbol{u}_i}{k} e^{(-(m_i/2qT_i)((\omega - k\cdot u_i)/k)^2)}\right)\right] \end{aligned} \tag{6}$$

The dispersion relation allows us to obtain the real and imaginary parts of the wave frequency:

$$\omega_r = \boldsymbol{u}_i \cdot \boldsymbol{k} + c_s k \tag{7}$$

$$\omega_i = \left(\frac{\pi}{8}\right)^{1/2} c_s k\left[\left(\frac{\boldsymbol{k}\cdot(\boldsymbol{u}_e - \boldsymbol{u}_i) - k c_s}{k v_e}\right) - \left(\frac{T_e}{T_i}\right)^{3/2} e^{-T_e/2T_i}\right] - \frac{\nu_i}{2} \tag{8}$$

where $c_s = \sqrt{qT_e/m_i}$, $v_e = \sqrt{qT_e/m_e}$. The latter result for the imaginary component of the frequency provides insight into the terms that damp or grow the acoustic modes. The first term on the right-hand side of Eq. (8) represents the growth of the wave from inverse Landau damping on the electron species. This is a collisionless process whereby the acoustic waves can gain energy at the expense of electron drift $\boldsymbol{u}_e$, provided that a resonant condition is satisfied: the electron drift in the direction of the phase velocity must exceed the wave speed in the ion frame of reference, c_s. This is inherently a kinetic effect and depends on an interaction of the waves with a small subset of the electron distribution of particles. The criterion for electron growth is typically satisfied for hollow cathode plasmas because they exhibit high electron drift in the plume. The second term in the imaginary part of ω represents collisionless damping of the waves from ion Landau damping. In a process that directly mirrors that of the electrons, the bulk ion population can remove energy from the acoustic turbulence oscillations due to the resonant interaction of a small subset of the ions in the distribution function moving at the wave phase velocity. The last term in Eq. (8) represents damping of the wave due to ion collisions.

Because the perturbed density scales with potential amplitude [Eq. (6)], the summations over $\boldsymbol{k}$ in the expressions for momentum and energy rates [Eqs. (1) and (4)] are weighted by the square of the potential amplitude ϕ_{1k}^2. Without a fully self-consistent description of the dominant processes governing the interaction of the ion–acoustic modes, it is not possible to know a priori how ϕ_{1k}^2 depends on the wave vector. We circumvent this limitation by assuming a functional form of the potential amplitude that is informed by experimental measurements and is consistent with theories for saturated or semisaturated acoustic turbulent spectra [23,35]:

$$\phi_{1k}^2 = \begin{cases} 0 & \omega_r > \beta\omega_{pi} \\ \delta(\hat{\boldsymbol{k}} - \hat{\boldsymbol{V}}_D) C_0 \omega_r^{-1} & \beta\omega_{pi} > \omega_r > \omega_0 \\ 0 & \omega_r < \omega_0 \end{cases} \tag{9}$$

where C_0 and β are constants; δ denotes the Dirac delta function; $\hat{\boldsymbol{V}}_D = (\boldsymbol{u}_e - \boldsymbol{u}_i)/|\boldsymbol{u}_e - \boldsymbol{u}_i|$ is the direction of relative drift between the species; $\omega_{pi} = \sqrt{q^2 n_0/(\varepsilon_0 m_i)}$ is the ion plasma frequency; and ω_0 is the lower-bound cutoff frequency for the instability. The inverse power law for the magnitude of the energy spectrum is consistent with a number of theoretical and experimental results of saturated or partially saturated IAT. It is the result of a redistribution of energy in the spectra to longer length scales by nonlinear processes [18,19]. The need for a lower cutoff frequency ω_0 for the spectrum is based on previous measurements of the IAT spectra in a 100 A LaB6 cathode (Fig. 3 in [23] and Fig. 5 in [25]) and is physically attributed to damping of acoustic modes at long length scales by processes such as geometric cutoffs or ion collisions [23]. The choice to place an upper bound on the spectrum at $\omega_r = \beta\omega_{pi}$ represents the theoretical cutoff of ion–acoustic waves above this frequency, and the scaling factor $\beta < 1$ captures the experimental observations from [23] that the acoustic modes actually dissipate at some fraction of this theoretical limit. The multiplication by the Dirac delta only selects wave vectors in the direction of relative drift. This choice is motivated by Eq. (8), which shows that the growth rate is maximized when k is collinear with $\boldsymbol{u}_e - \boldsymbol{u}_i$. We therefore assume that the wave direction is confined to a very narrow cone in this dominant direction.

Applying the definition for wave energy density of electrostatic modes [20] to the dielectric response for the ion–acoustic instability, we find that the perturbations of the plasma potential can be expressed as a function of the wave energy density W. For the kth mode of the ion–acoustic waves, W_k becomes

$$W_k = \frac{\omega_r}{k c_s}\left(\frac{n_0 q \phi_{1k}^2}{T_e}\right) \tag{10}$$

As we will find in the next subsection, it will be necessary to determine moments of the summation,

$$\sum_k (\omega_r)^l W_k$$

where l is an integer. To approximate this quantity, we convert the summation over k to an integral by multiplying by a differential Δk such that

$$\sum_k (\omega_r)^l W_k = \frac{1}{\Delta k}\int_{k_{\min}}^{k_{\max}} W_k (\omega_r)^l \, \mathrm{d}k \tag{11}$$

Because we have assumed a distribution in which the wave vector is collinear with the electron–ion drift velocity, the frequency and wavenumber are linearly related by $\omega_r = k c_s[1 + \hat{\boldsymbol{V}}_D \cdot \boldsymbol{u}_i/c_s]$. Evaluating this integral with the specified form of ϕ_{1k}^2 from Eq. (9), we find the result

$$\sum_k (\omega_r)^l W_k = \begin{cases} W_T \dfrac{\beta\omega_{pi}}{\ell_n[\beta\omega_{pi}/\omega_0]} & l = 1 \\ W_T & l = 0 \\ W_T \dfrac{1}{\omega_0\, \ell_n[\beta\omega_{pi}/\omega_0]} & l = -1 \end{cases} \tag{12}$$

where W_T denotes the total wave energy density summed over all k modes of the spectrum.

2. Wave Energy Equation

The plasma wave kinetic equation (cf. [20]) for the evolution of the kth electrostatic mode in the plasma is given by

$$\frac{\partial N_k}{\partial t} + \nabla \cdot (N_k \nabla_k \omega_r) - \nabla_k \cdot (N_k \nabla \omega_r) = 2\omega_i N_k \tag{13}$$

where $N_k = W_k/\omega_r$ denotes the wave action. This expression can be interpreted as a conservation equation for the density of quasi particles, phonons, at each wave vector. The first two terms on the left-hand side of Eq. (13) represent the flux of phonons in physical space, where they are convected out of the volume at the mode group velocity. The third term is an effective acceleration that results as varying background plasma parameters change the dispersion of the modes propagating at $\boldsymbol{k}$. This parallels the way the electric field term in the Vlasov equation changes the velocity of particles in a given distribution function through acceleration. The terms on the right side of Eq. (13) represent sources and sinks due to interactions with the plasma species. These include linear effects such as Landau damping and weak collisions [cf. Eq. (8)] and higher-order, nonlinear terms due to wave–wave and wave–particle coupling effects [22,36] that we have neglected.

Using the assumed distribution of wave amplitude and the explicit forms for ω_r and ω_i, we integrate Eq. (13) over all values of k to find

$$\begin{aligned}
&\frac{\partial W_T}{\partial t} + \nabla \cdot (W_T[c_s \hat{\boldsymbol{V}}_D + \boldsymbol{u}_i]) \\
&= W_T \left(\frac{\omega_0 \ell_n[\beta\omega_{pi}/\omega_0]}{1 + \hat{\boldsymbol{V}}_D \cdot \boldsymbol{u}_i / c_s} \left(\frac{\pi}{2}\right)^{1/2} \left[\frac{|\boldsymbol{u}_e - \boldsymbol{u}_i| - c_s}{v_e} - \left(\frac{T_e}{T_i}\right)^{3/2} e^{-T_e/2T_i} \right] \right. \\
&- \nu_i - \omega_0 \ell_n[\beta\omega_{pi}/\omega_0] \left(\frac{\partial}{\partial t} \left[\frac{1}{\omega_0 \ell_n[\beta\omega_{pi}/\omega_0]} \right] \right. \\
&\left. \left. + (c_s \hat{\boldsymbol{V}}_D + \boldsymbol{u}_i) \cdot \nabla \left[\frac{1}{\omega_0 \ell_n[\beta\omega_{pi}/\omega_0]} \right] \right) \right)
\end{aligned} \tag{14}$$

Because the acoustic modes propagate in the laboratory frame with group velocity $\partial\omega/\partial\boldsymbol{k} = c_s \hat{\boldsymbol{V}}_D + \boldsymbol{u}_i$, the last term in Eq. (14) represents the characteristic time scale in the wave frame of reference over which the parameter $\omega_0 \ell_n[\beta\omega_{pi}/\omega_0]$ varies. For this investigation, we assume that the cutoff frequency ω_0 is approximately constant and that the logarithmic contribution $\ell_n[\beta\omega_{pi}/\omega_0]$ is only a weakly varying parameter in the plume. We therefore can neglect this last term compared to the collisional damping and the growth. This allows us to write Eq. (14) in the simplified form

$$\begin{aligned}
&\frac{\partial W_T}{\partial t} + \nabla \cdot (W_T[c_s \hat{\boldsymbol{V}}_D + \boldsymbol{u}_i]) \\
&= \omega_0 W_T \left(\left(\frac{\pi}{2}\right)^{1/2} \left[\frac{|\boldsymbol{u}_e - \boldsymbol{u}_i| - c_s}{v_e} - \left(\frac{T_e}{T_i}\right)^{3/2} e^{-T_e/2T_i} \right] - \frac{\nu_i}{\omega_0} \right)
\end{aligned} \tag{15}$$

The interpretation of this equation is that the wave energy propagates along characteristics parallel to the average group velocity. This energy changes as it convects through the plasma depending on the interchange between growth from the electron drift and damping from resonant heating of ions and collisions. Equation (15) has, in fact, the form of a conservation statement and can be solved concurrently with the remainder of evolution equations in OrCa2D.

3. Momentum Equation for Ions and Electrons

For the change in momentum of the electrons, Eq. (1) yields

$$\boldsymbol{F}_{a(e)} = -\boldsymbol{F}_{a(i)} = -m_e n_0 \nu_a (\boldsymbol{u}_e - \boldsymbol{u}_i) \tag{16}$$

where we have defined an effective collision frequency

$$\begin{aligned}
\nu_a &= \sum_k \frac{kq\phi_k^2}{m_e T_e} \left(\frac{\pi}{2}\right)^{1/2} \left(\frac{m_e}{qT_e}\right)^{1/2} \\
&= \left[\frac{\beta}{\ell_n[\beta\omega_{pi}/\omega_0]} \left(\frac{\pi}{2}\right)^{1/2} \frac{1}{(1 + \hat{\boldsymbol{V}}_D \cdot \boldsymbol{u}_i / c_s)^2} \right] \omega_{pe} \frac{W_T}{n_0 T_e}
\end{aligned} \tag{17}$$

where $\omega_{pe} = \sqrt{q^2 n_0/(\varepsilon_0 m_e)}$ is the electron plasma frequency. The physical implication of this result is that the relative drift between species leads to the growth of the acoustic modes through inverse Landau damping on the electrons. The transfer of momentum to the turbulence from the electrons is represented in a macroscopic way as an enhanced drag on this species with anomalous collision frequency ν_a. The parameter $\beta < 1$ is assumed to be constant, and we know empirically that, for the IAT in the cathode plasma (cf. Fig. 3 in [23]), the logarithm of the ratio of the upper-bound to lower-bound cutoff frequencies is order unity. Similarly, typical ion velocities in cathode plumes have been measured to be 2–5 km/s [24,37] with electron temperatures of 2–5 eV [23,38–40]. We therefore have $(1 + \hat{V}_D \cdot \boldsymbol{V}_i/c_s) \sim O[1]$. With these order of magnitude estimates, we can reduce the term in brackets to a single parameter $\alpha < 1$ such that

$$\nu_a = \alpha \omega_{pe} \frac{W_T}{n_0 T_e} \tag{18}$$

Using the explicit form for the momentum change due to IAT from Eq. (16), we can write the momentum equation for ions and electrons (see, for instance [6]) as

$$\begin{aligned}
&\frac{\partial (m n_0 \boldsymbol{u})_i}{\partial t} + \nabla \cdot (m n_0 \boldsymbol{u}\boldsymbol{u})_i = n_0 q \boldsymbol{E} - \nabla p_i + \dot{m} \boldsymbol{u}_n \\
&\quad - n_0 m_i \left[\nu_{ie}(\boldsymbol{u}_i - \boldsymbol{u}_e) + \nu_{in}(\boldsymbol{u}_i - \boldsymbol{u}_n) - \frac{m_e}{m_i} \nu_a (\boldsymbol{u}_i - \boldsymbol{u}_e) \right]
\end{aligned} \tag{19}$$

$$\begin{aligned}
&0 = -n_0 q \boldsymbol{E} - n_0 q \boldsymbol{u}_e \times \boldsymbol{B} - \nabla p_e - n_0 m_e [(\nu_{ei} + \nu_a)(\boldsymbol{u}_e - \boldsymbol{u}_i) + \nu_{en} \boldsymbol{u}_e], \\
&\boldsymbol{u}_e \gg \boldsymbol{u}_n
\end{aligned} \tag{20}$$

4. Energy Equation for Ions and Electrons

Subject to the definitions and assumptions from Secs. II.A1 and II.A.2, we can rewrite the heating terms for the electrons and ions from Eq. (4) as

$$\begin{aligned}
Q_{a(e)} &= \frac{1}{(1 + \hat{\boldsymbol{V}}_D \cdot \boldsymbol{u}_i / c_s)} \sum_k \left[\frac{1}{2} \frac{\mathrm{d}W_k}{\mathrm{d}t} + 2\omega_{i(e)} W_k \right], \\
Q_{a(i)} &= \frac{1}{(1 + \hat{\boldsymbol{V}}_D \cdot \boldsymbol{u}_i / c_s)} \sum_k \left[\frac{1}{2} \frac{\mathrm{d}W_k}{\mathrm{d}t} - 2\omega_{i(i)} W_k \right] - \frac{\mathrm{d}\varepsilon_k}{\mathrm{d}t}
\end{aligned} \tag{21}$$

where we have isolated the contributions to the wave growth from Eq. (8):

$$\begin{aligned}
\omega_{i(e)} &= \left(\frac{\pi}{8}\right)^{1/2} c_s k \left(\frac{\boldsymbol{k} \cdot (\boldsymbol{u}_e - \boldsymbol{u}_i) - c_s}{k v_e} \right), \\
\omega_{i(i)} &= -\left(\frac{\pi}{8}\right)^{1/2} c_s k \left(\left(\frac{T_e}{T_i}\right)^{3/2} e^{-T_e/2T_i} - \nu_i \right)
\end{aligned} \tag{22}$$

Considering that the multiplying term is of order unity, the expressions in Eq. (21) lend themselves to a physical interpretation of the kinetic energy of each species associated with the wave dynamics. In particular, the first term in both $Q_{a(e)}$ and $Q_{a(i)}$ represents the sloshing motion of the particles necessary to carry the waves. For the ions, this oscillatory motion gives rise to the wave momentum, whereas for the electrons, the sloshing results from the need to preserve quasi neutrality. In both cases, the magnitude of the particle kinetic energy for the wave motion is directly tied to the wave energy: the larger amplitude the waves are, the higher the energy is from

oscillations of both species. The second terms in both lines of Eq. (21) capture the resonant, irreversible heating processes associated with each species. For the electrons, this takes the form of inverse Landau damping on this species. This is a kinetic process where a population of electrons in the distribution that are resonant with the phase velocity lose energy to the wave growth, thereby causing an effective cooling of the electrons. For the ions, the contribution of irreversible heating is due to ion Landau damping and ion collisions. The former is a kinetic process where a small population of ions in the tail of distribution that are resonant with the phase velocity experience an irreversible gain in energy. This removes energy from the waves and adds it to the ions.

By the same arguments we employed to simplify the anomalous collision frequency [Eq. (18)], we can approximate Eq. (21) as

$$Q_{a(e)} = -\frac{\alpha}{2}\omega_{pi} W_T \left(\frac{|\boldsymbol{u}_e - \boldsymbol{u}_i| - c_s}{v_e} + \left(\frac{T_e}{T_i}\right)^{3/2} e^{-T_e/2T_i} \right),$$
$$Q_{a(i)} = +\frac{\alpha}{2}\omega_{pi} W_T \left(\frac{|\boldsymbol{u}_e - \boldsymbol{u}_i| - c_s}{v_e} + \left(\frac{T_e}{T_i}\right)^{3/2} e^{-T_e/2T_i} \right) \tag{23}$$

where we have made the physically reasonable assumption that ion collision frequency is lower than the ion plasma frequency $\nu_i/\omega_{pi} \ll 1$, and we have dropped the contributions of the electrostatic terms in $Q_{a(i)}$ under the assumption that the growth rate is lower than the ion plasma frequency. In these simplified forms, we can see that the ion heating approximately balances the electron heating. The electrons therefore always lose energy to the growth of the waves. The ion population conversely always will be heated.

Written explicitly then, the energy equation for electrons (e.g., [6]) with contributions from the IAT thus becomes

$$\frac{3}{2}\frac{\partial p_e}{\partial t} + \nabla \cdot \left(\frac{5}{2} p_e \boldsymbol{u}_e - \kappa_e \nabla T_e \right) - \boldsymbol{u}_e \cdot \nabla p_e = Q_e^T + Q_{a(e)} + m_e n_0 (\nu_{ei} + \nu_a) \boldsymbol{u}_e \cdot (\boldsymbol{u}_e - \boldsymbol{u}_i) - \dot{n} q \varepsilon_{ip} \tag{24}$$

The terms on the right-hand side denote, in order, the heat exchange due to thermal nonequilibrium of electrons with ions and neutrals, the anomalous cooling, the friction heating, and the energy lost due to ionization, with ε_{ip} being the ionization potential.

We can compare the importance of anomalous cooling with respect to the other source terms. In particular, the ratio of the anomalous cooling and friction terms yields

$$\left| \frac{Q_{a(e)}}{m_e n \nu_a \boldsymbol{u}_e \cdot (\boldsymbol{u}_e - \boldsymbol{u}_i)} \right| \approx \frac{1}{2}\left(\frac{m_e}{m_i}\right)^{1/2} \left[\frac{\sqrt{qT_e/m_e}}{|\boldsymbol{u}_e|} + \frac{qT_e/m_e}{|\boldsymbol{u}_e|^2} \left(\frac{T_e}{T_i}\right)^{3/2} e^{-T_e/2T_i} \right] \tag{25}$$

For cathode plasmas that we have investigated in previous work [15,23,40], we have computed the ratio of the electron drift and thermal velocity to be at most of order unity, and because the square root of the mass ratios is ∼480 and the maximum value of the exponential contribution $(T_e/T_i)^{3/2}\exp(-T_e/2T_i) \approx 1.16$, we therefore can neglect the anomalous heating compared to the frictional heating by the anomalous collision frequency.

Finally, we apply the same treatment as before to derive the ion heating equation (e.g., [6]). However, this time, we find that we can neglect the resistive heating term in favor of the anomalous ion heating:

$$\frac{3}{2}\frac{\partial p_i}{\partial t} + \nabla \cdot \left(\frac{5}{2} p_i \boldsymbol{u}_i - \kappa_i \nabla T_i \right) - \boldsymbol{u}_i \cdot \nabla p_i = Q_i^T + Q_{a(i)} \tag{26}$$

The need to consider this expression for ion heating represents a significant departure from previous implementations of OrCa2D [5,6,12–15,26]. In these earlier versions, the energy equation for ions and neutrals was combined due to the short thermal equilibration time between the species. However, because we have assumed here that the growth rate of the instability $\omega_i \gg \nu_i$, the equilibration between species is no longer valid. Thus, separate evolution equations for the neutrals and ions must be considered. We can simplify Eq. (26) further by making a number of assumptions informed by experimental measurements in the cathode plume. In particular, a recent campaign to measure ion velocities along the centerline of a 100 A LaB_6 hollow cathode [24] has shown that the magnitude of the ion flow velocity varies slowly in the plume. We therefore make the assumption that $\nabla p_i/p_i \gg \nabla \cdot \boldsymbol{u}_i/\boldsymbol{u}_i$. Similarly, if we assume that the electron drift is sufficiently high that the growth from electrons dominates over the ion Landau damping (a valid approximation in most regions near the cathode), we can include Eq. (15) in Eq. (26) as

$$\frac{3}{2}\frac{\partial p_i}{\partial t} + \nabla \cdot \left(\frac{3}{2} p_i \boldsymbol{u}_e \right) = \frac{\alpha}{2}\frac{\omega_{pi}}{\omega_0}\left(\frac{2}{\pi}\right)^{1/2} \left[\frac{\partial W_T}{\partial t} + \nabla \cdot (W_T [c_s \hat{\boldsymbol{V}}_D + \boldsymbol{u}_i]) \right] \tag{27}$$

At steady state, which ultimately is the condition where the cathode equilibrates, and subject to the assumption that $c_s \sim |\boldsymbol{u}_i|$, we further can reduce this expression to

$$\nabla(nT_i) \approx \frac{\alpha}{q}\frac{\omega_{pi}}{\omega_0}\left(\frac{2}{\pi}\right)^{1/2} \nabla W_T \tag{28}$$

For the slowly varying plasma parameters in the cathode plume, ω_{pi}/ω_0 is approximately constant. In this case, we find the relation

$$T_i \approx \Gamma \frac{W_T}{n} \tag{29}$$

where Γ is a constant depending on the ratio of the plasma frequency to the cutoff frequency. This expression is in keeping with a physical description of the wave dynamics. Oscillations in the plasma density and ion velocity that correspond to the propagation of the acoustic modes lead to a time-averaged broadening in the standard deviation of the velocity (i.e., the temperature). The scaling indicated by Eq. (29) has been experimentally validated in the three most recent studies that have examined the relationship between IAT and ion energy in a high-current cathode plume [23,24,37].

B. Self-Induced Magnetic Field and Ohm's Law

Magnetic fields induced by the large current densities that can develop in high-current hollow cathodes cannot be neglected in numerical simulations. Figure 2 shows the two-dimensional (2-D) contour of the azimuthal magnetic field produced by the distribution of electron current density in a simulation of a LaB_6 hollow cathode operating at 140 A, according to Ampere's law:

$$B_\theta(z, r) = \frac{\mu_0}{2r}\int_0^r j_{e,z}(z, r') r' \, \mathrm{d}r' \tag{30}$$

This expression can be easily evaluated in OrCa2D. The maximum values are found in the vicinity of the orifice and reach more than 50 G. For reference, the typical applied magnetic fields along the axis of Hall thrusters are in the order of 150 G. In OrCa2D numerical simulations of cathodes with applied magnetic fields, we have observed that the plasma in the plume is altered significantly,

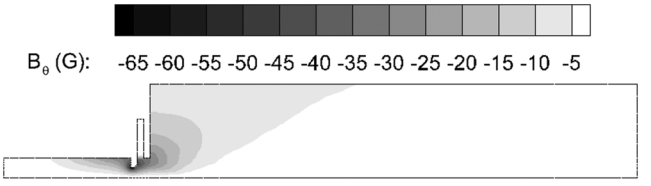

Fig. 2 Azimuthal self-induced magnetic field B_θ computed from Eq. (30).

making it much more confined around the axis. Thus, self-induced magnetic fields must be included in OrCa2D simulations of high-current cathodes.

We allow only for the azimuthal component of the magnetic field in our model because the electron current is mostly axial in the region of interest. This assumption also simplifies the process of solving for Ohm's law in OrCa2D. For a generic magnetic field in three dimensions, which can be the combination of the applied field in the axial–radial plane and a self-induced azimuthal magnetic field, Ohm's law reads

$$\begin{aligned}\theta \to 0 &= -\eta\Omega_e j_{e\perp} + \eta j_{e\theta},\\ // \to E_{//} &= -\frac{\nabla_{//}(n_0T_e)}{n_0} + \eta\Omega_e j_{e\perp}\beta_\theta + \eta j_{e//} + \eta_{ei} j_{i//},\\ \perp \to E_\perp &= -\frac{\nabla_\perp(n_0T_e)}{n_0} - \eta\Omega_e j_{e//}\beta_\theta + \eta(1+\Omega_e^2\beta_{//}^2) j_{e\perp} + \eta_{ei} j_{i\perp}\end{aligned} \tag{31}$$

where η, η_{ei}, and Ω are the electron resistivity, electron–ion resistivity, and Hall parameter, which are defined as

$$\eta = \frac{m_e(\nu_{en}+\nu_{ei}+\nu_a)}{nq^2}, \qquad \eta_{ei} = \frac{m_e(\nu_{ei}+\nu_a)}{nq^2},$$
$$\Omega_e = \frac{qB}{m_e(\nu_{en}+\nu_{ei}+\nu_a)}$$

In the preceding expressions, the parallel ($//$) and perpendicular ($\perp$) directions (second and third equation) refer to the projection of the magnetic field in the z–r plane (Fig. 1). We can invert Ohm's law to obtain closed expressions for the in-plane current density components:

$$\begin{aligned} j_{e//} &= \frac{1+\Omega_e^2\beta_{//}^2}{(1+\Omega_e^2)\eta}\left(-\nabla_{//}\phi + \frac{\nabla_{//}(n_0T_e)}{n_0} - \eta_{ei} j_{i//}\right)\\ &\quad - \frac{\Omega e\beta_\theta}{(1+\Omega_e^2)\eta}\left(-\nabla_\perp\phi + \frac{\nabla_\perp(n_0T_e)}{n_0} - \eta_{ei} j_{i_\perp}\right),\\ j_{e\perp} &= \frac{\Omega e\beta_\theta}{(1+\Omega_e^2)\eta}\left(-\nabla_{//}\phi + \frac{\nabla_{//}(n_0T_e)}{n_0} - \eta_{ei} j_{i//}\right)\\ &\quad + \frac{1}{(1+\Omega_e^2)\eta}\left(-\nabla_\perp\phi + \frac{\nabla_\perp(n_0T_e)}{n_0} - \eta_{ei} j_{i_\perp}\right)\end{aligned} \tag{32}$$

As mentioned previously in this section, the computational grid is aligned with the applied in-plane magnetic field to avoid cross-diffusion terms in the computation of the plasma potential. This would have been no longer possible if we had considered the self-induced magnetic field components in the z–r plane because the vector β would have changed from time step to time step. On the other hand, Eq. (32), which only accounts for the azimuthal self-induced field, can be solved in a fixed MFAM or in a generalized z–r grid if no applied magnetic field exists (i.e., $\beta_{//} = 0$). It can also be shown that this expression is equivalent to the classical expression for Ohm's law (cf. [15]) when $\beta_\theta = 0$.

III. Comparison Between Anomalous Collision Frequency Models and Experiments

OrCa2D has been extensively validated by experimental results [5,6,12,13,15,17]. Thus, we focus here on highlighting improvements in the solution produced by OrCa2D when the models described in Sec. II are implemented. We use as an example a case (high-current LaB_6 cathode operating at 140 A) for which OrCa2D only produced qualitative agreement with experiments [15] when equipped with the Sagdeev and Galeev model that assumes saturation of the IAT at all times [22]:

$$\nu_a \sim \omega_{pe}\frac{W_T}{n_0T_e} \sim \alpha\omega_{pe}\frac{T_e}{T_i}\frac{u_e}{v_e} = \alpha\omega_{pe}\frac{T_e}{T_i}M_e \sim \alpha\omega_{pi}\frac{T_e}{T_i}\frac{u_e}{c_s} \approx \alpha'\omega_{pi}\frac{u_e}{c_s} \tag{33}$$

In simulations with OrCa2D [5,6,12,15,26] that make use of the Sagdeev–Galeev model (33), anomalous heating of ions was not modeled based on first principles, and so the ratio T_e/T_i in Eq. (33) was included only phenomenologically and as part of the scaling coefficient α'. It should therefore be noted that, in subsequent comparisons with results from this model, the variation of T_e/T_i was not accounted for self-consistently.

Modifications in OrCa2D with respect to the model presented in [5,6,12,15,26] are as follow. The anomalous collision frequency is now calculated by means of Eq. (18). The wave energy density is computed using Eq. (15), which is hyperbolic in nature and is discretized with the same first-order-accurate implicit Euler scheme in time and HLL solver for convection terms that the transport equations for neutrals and ions employ. The ion temperature equation now includes an additional term given by Eq. (23). Finally, the plasma potential is still computed from the combination of the current continuity equation and Ohm's law, which now takes the form of Eq. (32). This equation is discretized in space making use of a centered scheme that is second-order accurate.

The numerical results shown in this paper are for a LaB_6 cathode operating at 140 A of discharge current and a mass flow rate of 10 sccm(0.9765 mg/s) of xenon. There exists a gap between the anode and cathode that allows for the insertion of probes for plasma measurements in the cathode plume. Relative dimensions of the cathode are given in Table 1. Measurements of the wave energy density based on the amplitude of the plasma oscillations were also obtained in this region. These measurements have an uncertainty of approximately 1–2 eV for the plasma potential and the electron temperature and a factor of 2 for the wave energy density. The discharge voltage during laboratory test in these conditions was 25.2 V. We specified the maximum emitter temperature to be 1733°C, at a location of approximately two-thirds of the length of the emitter. The emitter temperature close to the orifice wall is 1625°C. These values were derived from emitter temperature measurements for a slightly different operating condition (100 A, 12 sccm) [15]. The latter was achieved by acknowledging that, for a constant discharge current, larger emitter temperatures lead to increased electron emission. In turn, the plasma potential inside the cathode tube has to decrease to allow for an increased amount of return current to the emitter so that the net current from the emitter remains constant. In consequence, the emitter temperature can be determined by satisfying that the plasma potential agrees well with the experimental measurements at the cathode orifice. The values of the emitter temperature required at 140 A are higher than at 100 A, which is consistent with the experimental trends observed for other cathodes [41]. The keeper was operated in floating mode. We run OrCa2D in a way such that the discharge voltage and emitter temperature are fixed, whereas the parameter ω_0 in Eq. (15), which represents the lower bound cutoff for the frequency spectra, is determined so that the discharge current is 140 A. When the Sagdeev–Galeev model [Eq. (33)] is used, it is the value of α' that is determined to achieve the discharge current prescribed by the operating condition.

To gain insight on the effect of each of the aspects of the model, we present five different results (Table 2) for which the computed

Table 1 Axial location of cathode elements with respect to the cathode orifice

Element	z/L_{emitter}
Orifice entrance	0
Orifice exit	0.06
Keeper entrance	0.12
Keeper exit	0.18
Anode edge	1.28

Table 2 Summary to simulation cases; description of the model and cutoff frequency ω_0

Case number	Model	Ion heating	Self-induced magnetic field	ω_0, 1/s
1	Sagdeev–Galeev	No	No	N/A
2	Wave energy	No	No	$6.49 \cdot 10^5$
3	Wave energy	No	Yes	$9.24 \cdot 10^5$
4	Wave energy	Yes [Eq. (26)]	Yes	$3.12 \cdot 10^6$
5	Wave energy	Yes [Eq. (29)]	Yes	$3.39 \cdot 10^6$

values of plasma density, electron temperature, plasma potential, and anomalous collision frequency along the cathode centerline are depicted in Fig. 3. Case 1 results were obtained using the analytical Sagdeev–Galeev model [Eq. (33)]. Case 2 makes use of the self-consistent anomalous model but only considers the effect that the IAT has on the momentum [Eqs. (16) and (17)], neglecting ion heating. We do not consider here the effect of the self-induced magnetic field either. Case 3 includes the effect of a self-induced magnetic field but also neglects ion heating. Cases 4 and 5 include the effect of the self-induced field and anomalous heating, using the complete ion energy equation [Eq. (26)] and the simplified model [Eq. (29)], respectively.

In Fig. 3, we also include the experimental measurements in the cathode plume region. $z = 0$ is the cathode orifice entrance, and the z axis has been nondimensionalized with the emitter length. The locations of other elements of the cathode are summarized in Table 1. The experimental value of the anomalous collision frequency has been derived from direct experimental measurements of the plasma density, electron temperature, and wave energy density using Eq. (17). The experimental wave energy density is based on direct measurements of the spectra of plasma oscillations [23] and has a factor of 2 uncertainty. We have also included in Fig. 3 (top right) the profile of the classical collision frequency $\nu_{ei} + \nu_{en}$ to highlight the regions of the computational domain in which the anomalous collision frequency is the principal contributor to electron transport.

While solving energy density equation [Eq. (15)], it is necessary to specify a floor value for W_T. This is because the right-hand side of the equation is negative inside the cathode tube, which will result in $W_T \to 0$ as $t \to \infty$. When this happens, there cannot be wave growth even in regions where the growth rate is positive due to the convective nature of Eq. (15). The physical significance of the floor value W_0 is that it represents the random thermal motion of the ions spontaneously exciting acoustic modes. Our numerical tests reveal that the value of W_0 has minimal influence on the results [26], as long as the anomalous collision frequency computed from Eq. (17) with $W_T = W_0$ is less than the classical collision frequency (Fig. 3, top right) inside the cathode tube. In Fig. 4, we depict the wave energy density for the simulations that make use of Eq. (15). It is shown that W_T is at the floor value inside the cathode tube. Wave growth only occurs when the right-hand side of Eq. (15) becomes positive.

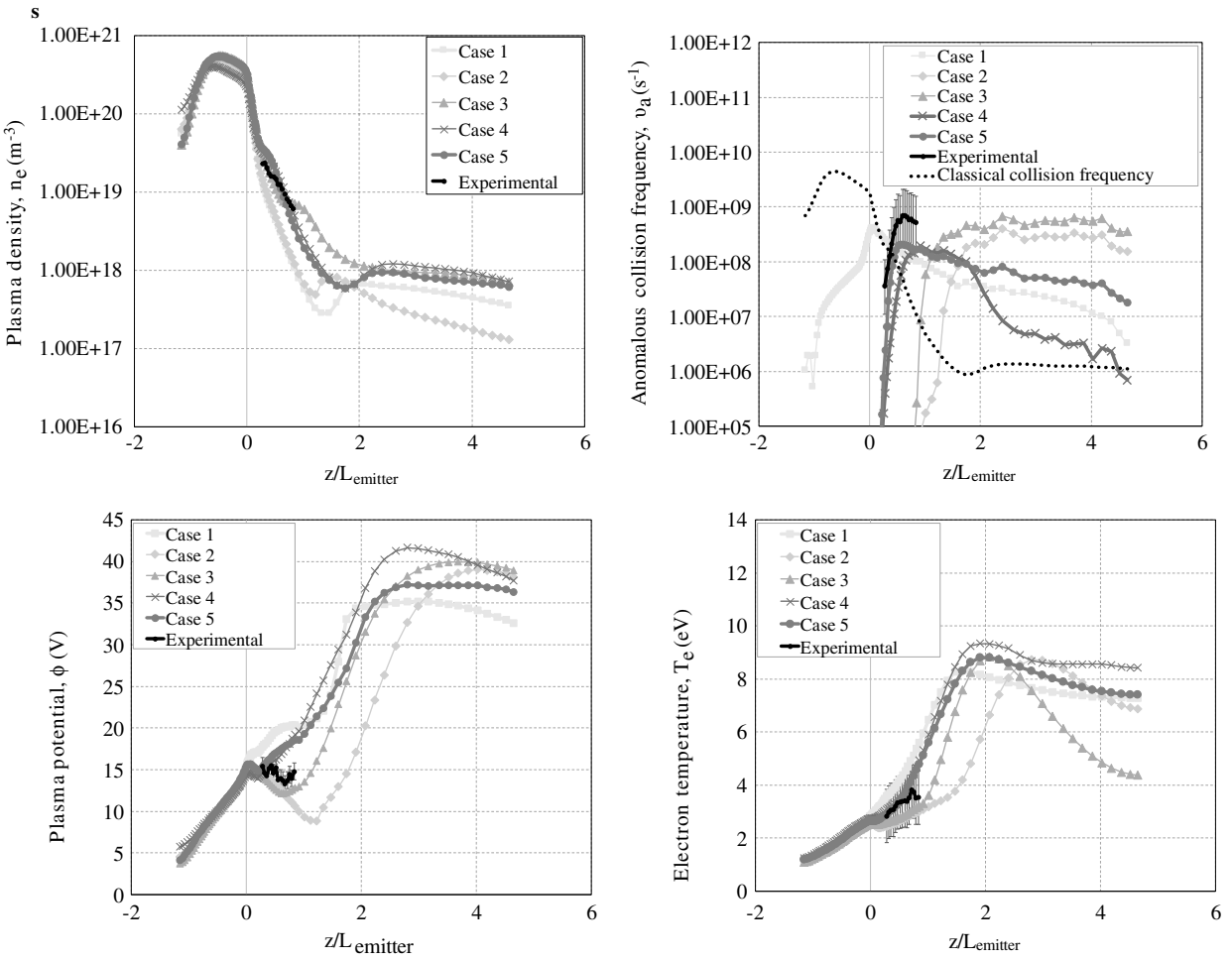

Fig. 3 Comparison between measured and computed plasma properties along the cathode centerline. The computed results are for the five different cases listed in Table 2.

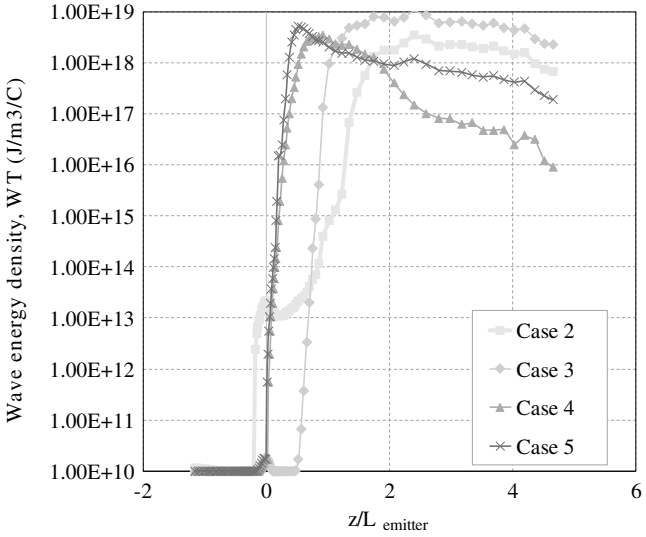

Fig. 4 Wave energy density values for cases 2–5 in Table 2.

A. Comparison Between Sagdeev–Galeev and Wave Energy Density Models for Electron Transport

The Sagdeev–Galeev model (case 1) accounts for the effect of saturated waves on the electron transport but not for ion heating. Thus, we can compare the latter directly with the wave energy density model (case 2) given by Eqs. (15) and (18). To achieve a discharge current of 140 A, $\alpha' = 0.013$ in Eq. (33). Using Eq. (33), we find that $\alpha' = \alpha T_e/T_i$. The value of α was determined (many years after the work reported in [22]) to be approximately 0.01 [42]. The latter suggests that the Sagdeev–Galeev model predicts the electron temperature to be approximately equal to the ion temperature as the instability saturates. We observe sharp differences in the anomalous collision frequency along the cathode centerline depending on the model employed. The Sagdeev and Galeev model predicts a peak in anomalous collision frequency at the orifice, whereas the wave energy approach predicts rapid growth in the orifice and saturation at approximately 1.5 emitter lengths from the peak of the Sagdeev and Galeev model. An explanation for such differences can be found by observing the nature of Eqs. (15), (18), and (33). Equation (33) is an algebraic expression that predicts large values of anomalous transport in regions in which the electron Mach number (the ratio of the drift velocity and the thermal velocity) and the plasma frequency are large. Figure 5 shows the distribution of the plasma density ($\omega_{pe} \sim \sqrt{n_e}$) and electron Mach number along the centerline for cases 1 and 2. For Eq. (33), the maximum anomalous collision frequency is achieved between the maxima of the plasma density and Mach number. As the density decreases by orders of magnitude, the maximum anomalous collision frequency is closer to the location of maximum plasma density (i.e., in the vicinity of the orifice), as shown in Fig. 3. On the contrary, Eq. (15) predicts large values of the growth rate when the electron Mach number is large. In the wave energy model, the wave energy density is small at the orifice because the conditions for growth are not met inside the cathode tube (Fig. 4). The growth rate is maximum at the orifice and immediately downstream of it, but because of the convective term in Eq. (15), the peak in the wave energy and, subsequently, in the anomalous collision frequency [Eq. (18)] occurs farther into the plume than in the Sagdeev–Galeev model. The significance of the comparison between these two models lies in the fact that the Sagdeev–Galeev model is limited by the assumption of saturation everywhere. In the orifice, the wave density model suggests that the waves are starting to grow, whereas the Sagdeev–Galeev model is assuming that these waves have reached saturation. Comparison with the experimental data (Fig. 3) reveals that neither model can predict the location of maximum anomalous collision frequency accurately, which appears to be located in between the predicted results for cases 1 and 2. We also observe large differences in plasma potential end electron temperature as a consequence of the change in the distribution of the anomalous collision frequency. Case 2 exhibits a characteristic kink in the plasma potential between $z/L_{\text{emitter}} = 0$ and $z/L_{\text{emitter}} = 1$ that does not occur when the Sagdeev–Galeev model is employed. This feature can be explained by the absence of significant anomalous collision frequency between $z/L_{\text{emitter}} = 0$ and $z/L_{\text{emitter}} = 1$ in the self-consistent model. Thus, the electrons experience low resistivity to their motion in the axial direction, and the plasma potential does not have to increase to support the electron current to the anode. In the Sagdeev–Galeev model, the resistivity in this region is close to its maximum, and the plasma potential has to monotonically increase to support the transport of electrons. Experimental measurements suggest that the plasma potential remains relatively flat in the region between $z/L_{\text{emitter}} = 0$ and $z/L_{\text{emitter}} = 1$, which is closer to the result produced by the wave energy model. We also observe that the predicted plasma density for both cases falls below the measured values by almost an order of magnitude at $z/L_{\text{emitter}} \sim 1$. This discrepancy between simulations and experiments is addressed in the next subsection.

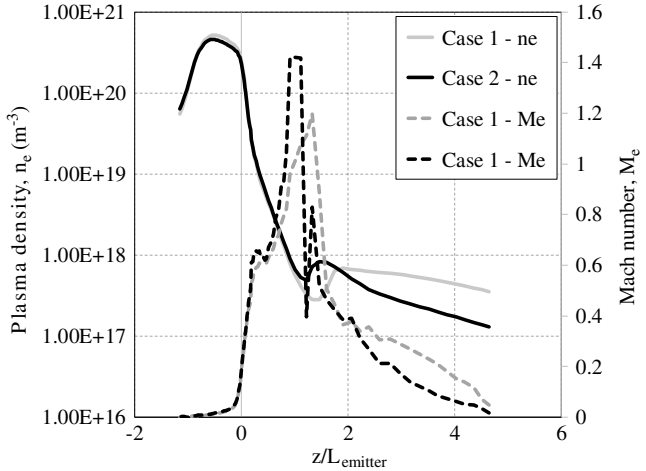

Fig. 5 Plasma density and electron Mach number ($M_e = u_e/v_e$) along the cathode centerline for cases 1 and 2 in Table 2.

B. Self-Induced Magnetic Field (Comparison Between Cases 2 and 3)

The effect of including the self-induced magnetic field in our simulations (Sec. II.B) is that the plasma density downstream of the cathode orifice increases along the cathode centerline due to magnetic confinement. With this improvement included in OrCa2D, we are able to produce simulations that exhibit much better agreement with the experimental measurements (Fig. 3, upper left) of the plasma density. Figure 6 shows 2-D contours of the plasma density with and without the self-induced magnetic field. The ion beam expands almost isotropically when no magnetic field is present. When the model for B_θ is included, the beam expands predominantly in the axial direction.

With respect to the anomalous collision frequency, its maximum value, as computed by the wave energy model, occurs slightly upstream compared to the result with no magnetic field. Even though the electron Mach number, which controls the growth rate of Eq. (15), decreases in a more confined beam (i.e., for the same electron current, the plasma density increases, resulting in a lower electron drift velocity), the value of the cutoff frequency ω_0 that is required to meet the operating condition of 140 A (Table 2) is higher than the one computed in the simulation with no magnetic field. A higher value of ω_0 increases the growth rate [Eq. (15)] in the vicinity of the orifice, which results in the wave energy density W_T reaching its maximum value more quickly than in case 2 (Fig. 4). In turn, the maximum anomalous collision frequency for case 3 is closer (but still upstream) to the location predicted by the measurements. We also observe that, for case 3, the electron temperature and plasma potential values agree remarkably well with the experimental measurements. It is worth noting (even though it is not shown here) that if the Sagdeev–Galeev model is employed when also accounting for the self-induced

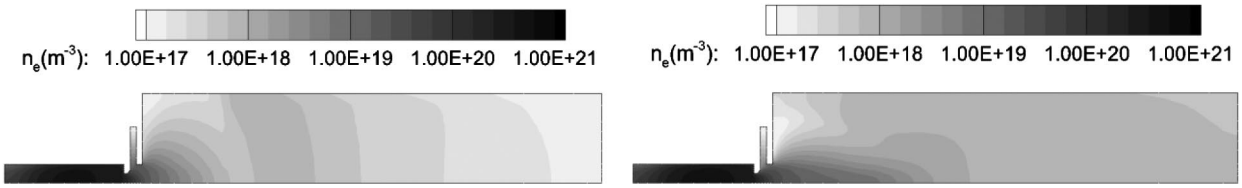

Fig. 6 Plasma density in LaB_6 cathode operating at 140 A and 10 cm^3 without self-induced magnetic field (left) and with self-induced magnetic field (right).

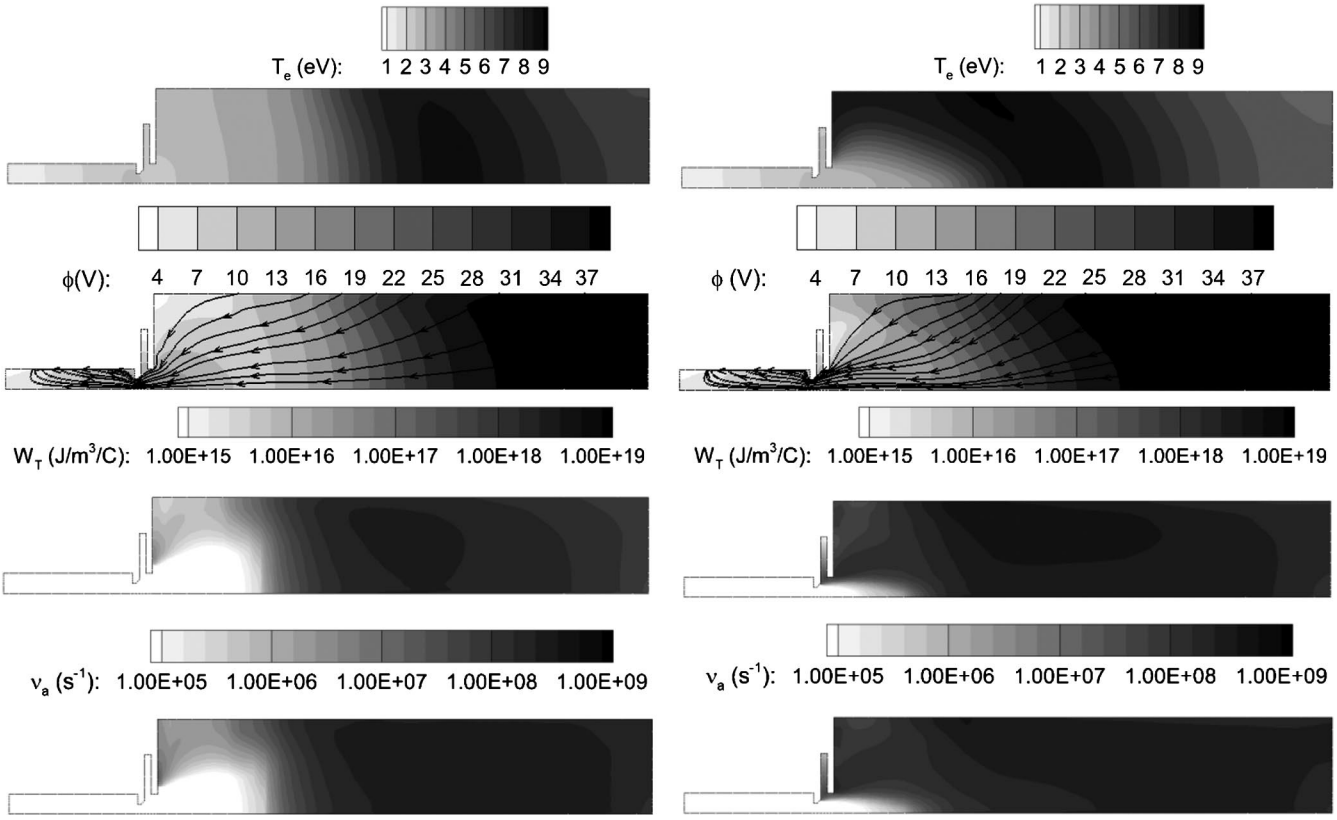

Fig. 7 2-D contour plots for plasma parameters. Left: no self-induced magnetic field (case 2 in Table 2), right: with self-induced magnetic field (case 3 in Table 2).

magnetic field, the comparison with the measured plasma density also improves with respect to case 1. However, the location of the maximum anomalous collision frequency will not move significantly because the conditions that produce a maximum value of Eq. (33) still occur in the vicinity of the orifice (i.e., most of the effect of the self-induced magnetic field occurs in the keeper and near plume because the plasma at the orifice is already confined by the small orifice cross section). Moreover, the limitation of the Sagdeev–Galeev model of predicting wave saturation at a location in which waves are only starting to grow is still applicable when we account for the self-induced magnetic field.

We show in Fig. 7 the 2-D contours of the relevant plasma parameters in simulations with and without the model for a self-induced magnetic field. The confinement of the plasma around the cathode axis is evident, with plasma properties closely following the plasma density contours of Fig. 6. We also observe that the electron streamtraces are closely parallel to the longitudinal axis immediately downstream of the orifice. In the region farther downstream, the effects of the self-induced magnetic field are negligible, as indicated by the 2-D distribution of B_θ in Fig. 2.

C. Effect of Ion Heating (Cases 4 and 5)

We finally consider the effect of ion heating due to the ion–acoustic turbulence. Figure 8 shows the ion temperature computed from Eqs. (26) and (29), corresponding to cases 4 and 5 in Table 2, respectively. The ion temperature reaches a maximum value of approximately 2 eV along the cathode centerline. Differences between the values computed from Eqs. (26) and (29) can be explained by the influence, albeit small, of the thermal conductivity. The latter leads to a more diffused distribution of the ion temperature for case 4. At the location of the maximum ion temperature, the solution with no anomalous heating predicts a temperature of 0.02 eV. The electron temperature at that location is 4 to 6 eV. It can be shown that the Landau damping term in Eq. (15) has a maximum when the ratio of the electron to the ion temperature is 3. As shown in Fig. 9, this ratio in our simulations is between 1.5 and 3 in the cathode plume, and thus we must expect significant differences with respect to the result of case 3, which did not account for ion heating. As shown in Figs. 3 and 10, when comparing case 3 with cases 4 and 5, the profiles of wave energy density and anomalous collision frequency respond by moving upstream for cases 4 and 5. In cases 4 and 5, the anomalous collision frequency decreases downstream of the peak instead of remaining approximately constant as in case 3. In the latter, the wave energy density stays constant in the plume because the growth and Landau damping terms in Eq. (15) are small. In cases 4 and 5, Landau damping is not negligible and reduces the wave energy density (Fig. 4) in regions of the plume ($z/L_{\text{emitter}} > 1$) where it is dominant over the growth term. We can find an explanation to the change in location of the maximum anomalous collision frequency by noting that, because the discharge current and voltage stay constant between simulations, the amount of anomalous resistivity

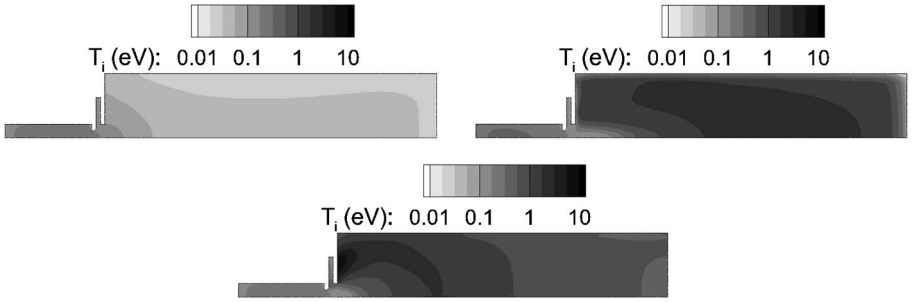

Fig. 8 2-D contour plots for ion temperature. Top left: no anomalous ion heating, top right: with anomalous ion heating, computed from Eq. (26), bottom: with anomalous ion heating, computed from Eq. (29).

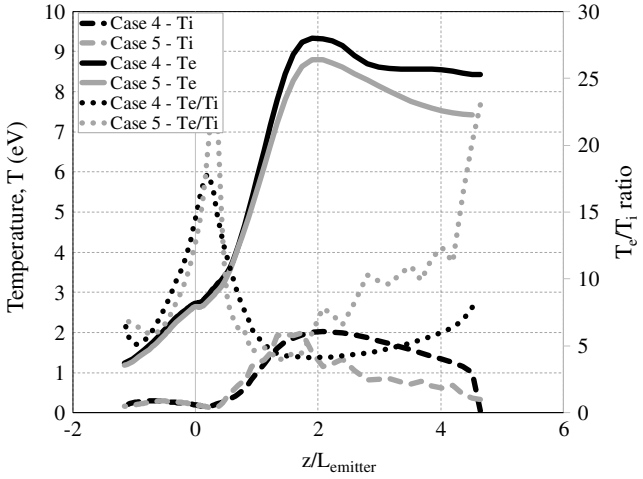

Fig. 9 Centerline profiles of electron and ion temperatures for cases 4 and 5 (refer to Table 2).

integrated along the electrons' path between the cathode and anode must remain approximately constant. Because the wave energy density and in turn the resistivity are lower in the plume in cases 4 and 5 than in case 3, we need higher resistivity (higher anomalous collision frequency) in locations upstream of where the Landau damping decreases the wave energy. The only way to achieve this in our simulations is to increase the cutoff frequency ω_0, as shown in Table 2, to promote growth of the instability. As the growth rate increases, the maximum anomalous collision frequency is reached farther upstream. Thus, we find that the location of the maximum anomalous collision frequency in simulations with ion heating (cases 4 and 5) is very close to the experimental location. Small changes are also observed between cases 3, 4, and 5 in the electron temperature, plasma potential, and plasma density as a consequence of the different anomalous collision frequency distribution. However, the numerical results still agree reasonably well with the measured quantities. The numerical results using the complete ion temperature equation and the simplified expression [Eq. (29)] are remarkably close. The validity of Eq. (29), at least for cathodes operating at high-current conditions have also been confirmed experimentally in [24,37], where laser-induced fluorescence was used to determine the distribution function of the ions at multiple axial locations in the cathode plume. We finally note that the ratio of the electron and ion temperatures (Fig. 9) is higher at the location of maximum anomalous collision frequency ($z/L_{\text{emitter}} \sim 1$) than the value predicted by the Sagdeev–Galeev model. In the Sagdeev–Galeev model, the coefficient employed in our simulation suggested that the ratio is close to 1, whereas the wave energy density model predicts a ratio of approximately 4. It should be recognized here that the value of 1 associated with the Sagdeev–Galeev model is a consequence of the assumption in Eq. (33) that T_e/T_i does not vary significantly, which naturally leads to some effective value after α' is determined. The physical meaning of this value and the location at which it occurs is therefore ambiguous. A more meaningful comparison would have been allowed if the self-consistently computed ion temperature from the solution of the ion energy equation was used in Eq. (33). However, this was beyond the scope of this paper. Nevertheless, at least from a numerical perspective, the discrepancy between models can be attributed to the shift in the location of maximum anomalous collision frequency between simulations.

We must discuss briefly the significance of the values of ω_0 summarized in Table 2 for each simulation. According to Eq. (9), ω_0 represents the lower bound at which the ion–acoustic instability develops. We assumed in our simulations that the value of ω_0 remains constant in space. Thus, it must be lower than the ion plasma frequency, at least in the regions of growth of the instability. The density distribution found in the simulations (Fig. 3) translates into plasma frequencies in the order of 10^8–10^9 s^{-1} in the cathode orifice and plume. These values are higher than any ω_0 found in simulations,

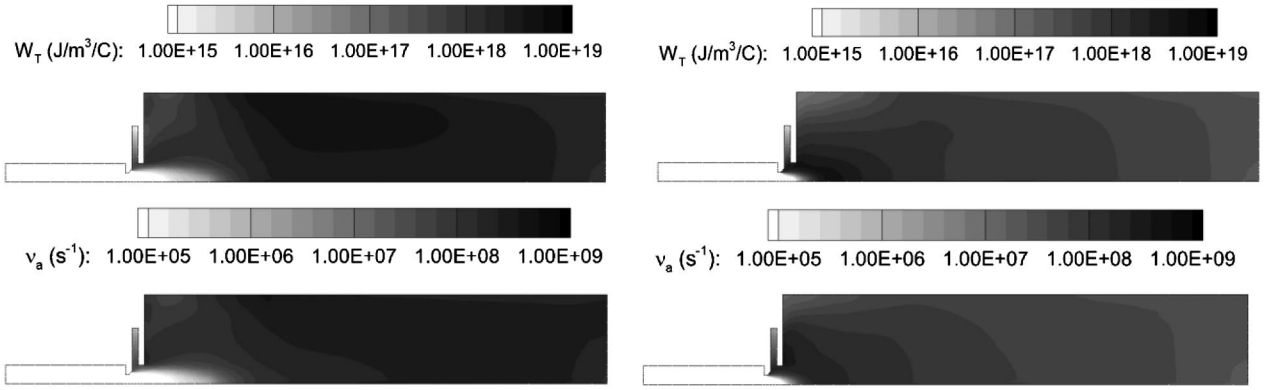

Fig. 10 2-D contour plots for wave energy density and anomalous collision frequency. Left: no anomalous ion heating (case 3 in Table 2), right: with anomalous ion heating (case 4 in Table 2).

and therefore the condition that ω_0 cannot exceed the ion plasma frequency is met. In addition, the values of ω_0 obtained in our simulations are similar to the wave frequencies that experimental data showed in Fig. 3 of [23] for multiple operating conditions (note that the 140 A condition is not shown).

IV. Conclusions

In this paper, a mathematical model was presented that yields the growth and saturation of the ion–acoustic turbulence (IAT) in the plume of hollow cathodes and its effect on the plasma resistivity and ion heating. Also included were the effects of self-induced magnetic fields, which are important in cathodes operating at large discharge currents. Numerical simulations that employed these models show large improvements in the agreement with plasma measurements with respect to a previous model, which assumed complete saturation of the instability and did not account for its growth stage and the anomalous heating of ions by the IAT.

The wave energy density was derived from a quasi-linear formulation of the Boltzmann equation for ions and electrons, combined with the dispersion relation for the IAT. The equation for its evolution thus takes the form of a partial differential equation that is hyperbolic in nature. The convection term depends on the group velocity, and the right-hand side of the equation controls the local growth or damping of the instability. The wave energy density was then related to the macroscopic effects of the IAT through a drag term in the momentum equation and a heating term in the energy equations for electrons and ions. These equations were then solved concurrently with the equations of motion of neutrals, ions, and electrons in the hollow cathode code OrCa2D.

The results produced by this model were compared with experimental measurements in the plume of a LaB_6 cathode operating at a discharge current of 140 A and mass flow rate of 10 sccm. At such high currents, it was found that the self-induced magnetic field could not be neglected, and so Ampere's and Ohm's laws were incorporated appropriately to take its effects into account. Numerical simulations showed that the growth rate of the instability reaches a maximum in the vicinity of the cathode orifice (as shown by a rapid increase in the wave energy density), but the resistivity reaches a maximum farther downstream in the plume. This occurs because the convective term in the wave energy density equation shifts the location of maximum resistivity downstream of the location of maximum growth. It was shown that the location and magnitude of the maximum anomalous collision frequency show close agreement with experimental measurements, especially when anomalous heating of ions is included. It was also shown that anomalous heating is the leading term in the ion temperature equation, allowing to formulate a simple linear relation between the wave energy density and the ion temperature. This relation has recently been confirmed experimentally. Finally, accounting for the self-induced magnetic field resulted in numerical solutions that showed significant plasma confinement in the proximity of the cathode centerline downstream of the orifice, in agreement with experimental observations.

Acknowledgments

The research described in this paper was carried out by the Jet Propulsion Laboratory, California Institute of Technology, under a contract with NASA. The support of NASA's Space Technology Mission Directorate through the Solar Electric Propulsion Technology Demonstration Mission project is gratefully acknowledged.

References

[1] Brophy, J. R., Friedman, L., and Culick, F., "Asteroid Retrieval Feasibility," *Proceedings of the 2012 Aerospace Conference*, Big Sky, MT, 2012, pp. 1–16. doi:10.1109/AERO.2012.6187031

[2] Brophy, J. R., and Oleson, S., "Spacecraft Conceptual Design for Returning Entire Near-Earth Asteroids," *48th AIAA/ASME/SAE/ASEE Joint Propulsion Conference & Exhibit*, AIAA Paper 2012-4067, July–Aug. 2012.

[3] Polk, J. E., Anderson, J., Brophy, J., Rawlin, V., Patterson, M., Sovey, J., and Hamley, J., "An Overview of the Results from an 8200-Hour Wear Test of the NSTAR Ion Thruster," *35th Joint Propulsion Conference and Exhibit*, AIAA Paper 1999-2446, July 1999.

[4] Sengupta, A., Brophy, J. R., and Goodfellow, K. D., "Status of the Extended Life Test of the Deep Space I Flight Spare Ion Engine After 30,352 Hours of Operation," AIAA Paper 2003-4558, July 2003.

[5] Mikellides, I. G., Katz, I., Goebel, D. M., Jameson, K. K., and Polk, J. E., "Wear Mechanisms in Electron Sources for Ion Propulsion II: Discharge Hollow Cathodes," *Journal of Propulsion of Power*, Vol. 24, No. 4, 2008, pp. 866–879. doi:10.2514/1.33462

[6] Mikellides, I. G., Katz, I. D., Goebel, D. M., and Polk, J. E., "Hollow Cathode Theory and Experiment II: A Two-Dimensional Theoretical Model of the Emitter Region," *Journal of Applied Physics*, Vol. 98, No. 11, 2005, Paper 113303. doi:10.1063/1.2135409

[7] Polk, J. E., Mikellides, I. G., Katz, I., and Capece, A. M., "Tungsten and Barium Transport in the Internal Plasma of Hollow Cathodes," *Journal of Applied Physics*, Vol. 105, No. 11, 2009, Paper 113301. doi:10.1063/1.3111970

[8] Polk, J. E., Mikellides, I. G., Capece, A. M., and Katz, I., "Barium Depletion in Hollow Cathode Emitters," *Journal of Applied Physics*, Vol. 119, No. 2, 2016, Paper 023303. doi:10.1063/1.4938489

[9] Brophy, J. R., and Garner, C., "Test of High Current Hollow Cathodes for Ion Engines," *24th Joint Propulsion Conference*, AIAA Paper 1988-2913, July 1988.

[10] Polk, J. E., Anderson, J. R., Brophy, J. R., Rawlin, V. K., Patterson, M. J., Sovey, J., and Hamley, J., "An Overview of the Results from an 8200 Hour Wear Test of the NSTAR Ion Thruster," *35th Joint Propulsion Conference and Exhibit*, AIAA Paper 1999-2446, June 1999.

[11] Sengupta, A., Brophy, J. R., Anderson, J. R., Garner, C., de Groh, K., Karniotis, T., and Banks, B., "An Overview of the Results from the 30,000 Hr Life Test of Deep Space 1 Flight Spare Ion Engine," *40th AIAA/ASME/SAE/ASEE Joint Propulsion Conference and Exhibit*, AIAA Paper 2004-3608, July 2004.

[12] Mikellides, I. G., Katz, I., Jameson, K. K., and Goebel, D. M., "Numerical Simulations of a Hall Thruster Hollow Cathode Plasma," *Proceedings of the 30th International Electric Propulsion Conference*, Electric Rocket Propulsion Soc. Paper IEPC-2007-018, Florence, Italy, Sept. 2007.

[13] Mikellides, I. G., Katz, I., Goebel, D. M., Polk, J. E., and Jameson, K. K., "Evidence of Non-Classical Plasma Transport in Hollow Cathodes for Electric Propulsion," *Journal of Applied Physics*, Vol. 101, No. 6, 2007, Paper 063301. doi:10.1063/1.2710763

[14] Mikellides, I. G., and Katz, I., "Wear Mechanisms in Electron Sources for Ion Propulsion I: Neutralizer Hollow Cathode," *Journal of Propulsion and Power*, Vol. 24, No. 4, 2008, pp. 855–865. doi:10.2514/1.33461

[15] Mikellides, I. G., Goebel, D. M., Jorns, B. A., Polk, J. E., and Guerrero, P., "Numerical Simulations of the Partially-Ionized Gas in a 100-A LaB6 Hollow Cathode," *IEEE Transactions on Plasma Science, Special Issue on Plasma Propulsion*, Vol. 43, No. 1, 2015, pp. 173–184. doi:10.1109/TPS.2014.2320876

[16] Mikellides, I. G., "Effects of Viscosity in a Partially-Ionized Channel Flow with Thermionic Emission," *Physics of Plasmas*, Vol. 16, No. 1, 2009, Paper 013501. doi:10.1063/1.3056397

[17] Mikellides, I. G., Katz, I., Goebel, D. M., and Polk, J. E., "Theoretical Model of a Hollow Cathode Insert Plasma," *40th AIAA/ASME/SAE/ASEE Joint Propulsion Conference and Exhibit*, AIAA Paper 2004-3817, July 2004.

[18] Bychenkov, V. Y., Silin, V. P., and Uryupin, S. A., "Ion–Acoustic Turbulence and Anomalous Transport," *Physics Reports*, Vol. 164, No. 3, 1988, pp. 119–215. doi:10.1016/0370-1573(90)90122-I

[19] de Kluvier, H., Perepelkin, N. F., and Hirose, A., "Experimental Results on Current-Driven Turbulent Plasmas—A Survey," *Physics Reports*, Vol. 199, No. 6, 1991, pp. 281–381. doi:10.1016/0370-1573(91)90060-Y

[20] Stix, T. H., *Waves in Plasmas*, Springer–Verlag, New York, 1992, Chap. 3.

[21] Horton, H., *Turbulent Transport in Magnetized Plasmas*, World Scientific, Singapore, 2012, Chap. 2.9.

[22] Sagdeev, R. Z., and Galeev, A., *Nonlinear Plasma Theory*, W. A. Benjamin, New York, 1969, pp. 94–103, Chap. III-2.

[23] Jorns, B. A., Mikellides, I. G., and Goebel, D. M., "Ion Acoustic Turbulence in a 100-A LaB6 Hollow Cathode," *Physical Review E*, Vol. 90, No. 6, 2014, Paper 063106. doi:10.1103/PhysRevE.90.063106

[24] Dodson, D. A., Perez Grande, D., Jorns, B. A., and Goebel, D. M., "Laser-Induced Fluorescence Measurements of Energetic Ions in a 100-A LaB6 Hollow Cathode," *52nd AIAA/SAE/ASEE Joint Propulsion Conference*, AIAA Paper 2016-4838, July 2016.

[25] Jorns, B. A., Mikellides, I. G., Goebel, D. M., and Lopez Ortega, A., "Mitigation of Energetic Ions and Keeper Erosion in a High-Current Hollow Cathode," *Proceedings of the 34th International Electric Propulsion Conference*, Electric Rocket Propulsion Soc. Paper IEPC-2015-134, Hyogo-Kobe, Japan, July 2015.

[26] Lopez Ortega, A., Mikellides, I. G., and Jorns, B. A., "First-Principles Modeling of IAT-Driven Anomalous Resistivity in Hollow Cathode Discharges II: Numerical Simulations and Comparisons with Experiments," *52nd AIAA/SAE/ASEE Joint Propulsion Conference*, AIAA Paper 2016-4627, July 2016.

[27] Toro, E. F., *Riemann Solvers and Numerical Methods for Fluid Dynamics: A Practical Introduction*, Springer, New York, 1999, p. 315, Chap. 10.

[28] Lopez Ortega, A., and Mikellides, I. G., "A New Cell-Centered Implicit Numerical Scheme for Ions in the 2-D Axisymmetric Code Hall2De" *50th AIAA/ASME/SAE/ASEE Joint Propulsion Conference*, AIAA Paper 2014-3621, July 2014.

[29] Marchand, R., and Dumberry, M., "CARRE: A Quasi-Orthogonal Mesh Generator for 2D Edge Plasma Modelling," *Computer Physics Communications*, Vol. 96, Nos. 2–3, 1996, pp. 232–246. doi:10.1016/0010-4655(96)00052-5

[30] Lin, Z., Hahm, T. S., Lee, W. W., Tang, W. M., and White, R. B., "Turbulent Transport Reduction by Zonal Flows: Massively Parallel Simulations," *Science*, Vol. 281, No. 5384, 1998, pp. 1835–1837. doi:10.1126/science.281.5384.1835

[31] Dushman, S., "Electron Emission from Metals as a Function of Temperature," *Physical Review*, Vol. 21, No. 6, 1923, pp. 623–636. doi:10.1103/PhysRev.21.623

[32] Dum, T., "Can We Find Useful Algorithms for Anomalous Transport?" *Cross-Scale Coupling in Space Plasmas*, edited by J. L. Horwitz, N. Singh, and J. L. Burch, American Geophysical Union, Washington, D.C., 1995, pp. 1–12. doi:10.1029/GM093p0001

[33] Davidson, R., and Krall, N., "Anomalous Transport in High-Temperature Plasmas with Applications to Solenoidal Fusion Systems," *Nuclear Fusion*, Vol. 17, No. 6, 1977, pp. 1313–1372. doi:10.1088/0029-5515/17/6/017

[34] Jorns, B. A., Lopez Ortega, A., and Mikellides, I. G., "First-Principles Modeling of IAT-Driven Anomalous Resistivity in Hollow Cathode Discharges I: Theory," *52nd AIAA/SAE/ASEE Joint Propulsion Conference*, AIAA Paper 2016-4626, July 2016.

[35] Tsytovich, N., *Theory of Turbulent Plasma*, Series Studies in Soviet Science, Springer, New York, 1977, pp. 192–195, Chap. 7.6.

[36] Davidson, R., *Methods in Nonlinear Plasma Theory*, Academic Press, New York, 1972, Chaps. 12, 14.

[37] Williams, G., Smith, T., Domonkos, M., Gallimore, A., and Drake, R., "Laser Induced Fluorescence Characterization of Ions Emitted from Hollow Cathodes," *IEEE Transactions on Plasma Science*, Vol. 28, No. 5, 2000, pp. 1664–1675. doi:10.1109/27.901252

[38] Chu, E., and Goebel, D. M., "High-Current Lanthanum Hexaboride Hollow Cathode for 10-to-50-kW Hall Thrusters," *IEEE Transactions on Plasma Science*, Vol. 40, No. 9, 2012, pp. 2133–2144. doi:10.1109/TPS.2012.2206832

[39] Jameson, K. K., Goebel, D. M., and Watkins, R., "Hollow Cathode and Keeper-Region Plasma Measurements," *41st AIAA/ASME/SAE/ASEE Joint Propulsion Conference & Exhibit*, AIAA Paper 2005-3667, July 2005.

[40] Jorns, B. A., Goebel, D. M., and Mikellides, I. G., "Investigation of Energetic Ions in a 100-A Hollow Cathode," *50th AIAA/ASME/SAE/ASEE Joint Propulsion Conference*, AIAA Paper 2014-3826, July 2014.

[41] Polk, J. E., Goebel, D. M., and Guerrero, P., "Thermal Characteristics of a Lanthanum Hexaboride Hollow Cathode," Electric Rocket Propulsion Soc. Paper IEPC-2015-44, July 2015.

[42] Tsytovich, V. N., *Lectures on Non-Linear Plasma Kinetics*, Springer–Verlag, Berlin, 1995, p. 195.

L. B. King
Associate Editor